



Assessment of two fluidic actuators for active flow control on a one-sided diffuser

A modal analysis

B. Steinfurth¹ · F. Haucke¹ · J. Weiss¹

Received: 20 February 2018 / Revised: 2 October 2018 / Accepted: 10 October 2018 / Published online: 1 November 2018
© Deutsches Zentrum für Luft- und Raumfahrt e.V. 2018

Abstract

The manipulated flow along a one-sided diffuser is investigated experimentally by means of particle image velocimetry and wall pressure measurements. Two fluidic actuators are considered: a fluidic diverter emitting two alternately pulsed jets and a fluidic oscillator generating one spatially oscillating jet. Active separation control is performed with these devices to suppress the pressure-induced separation bubble present in the uncontrolled flow field. The method of proper orthogonal decomposition is employed to identify inherent physical mechanisms subject to varied jet emission angles as well as actuation intensities and construct a reduced order model by utilizing modal coefficients to obtain phase information regarding the periodic actuation process. As a main result, we show that longitudinal vortex structures determining the separation control capability, are more distinct for the fluidic oscillator. Furthermore, the flow fields manipulated by both actuators at a low momentum input are dominated by a spatial mode resembling the base flow. However, this feature is suppressed by the fluidic diverter at greater velocity ratios, whereas the variation of actuation intensity does not yield significant alterations to the spatial modes observed for the fluidic oscillator.

Keywords Active flow control · Fluidic actuators · Proper orthogonal decomposition · Pressure induced flow separation

1 Introduction

Fluidic actuators are well established within the Active Flow Control community. They are deployed to generate unsteady jets based on their internal geometries, boasting advantages that come in the form of an absence of moving parts and electrical supply system when compared to conventional devices, such as solenoid valves. This makes them robust, reliable and relatively easy to fabricate in comparison. Their field of application includes film cooling [8], mixing enhancement [6] and active separation control (ASC) [15] with the latter being the focus of this article.

The one-sided diffuser, along with the backward facing ramp, represents a generic flow configuration relevant to various applications in public transportation, such as wings, road vehicle backlights and combustion chambers of aircraft engines. Consequently, it is object of various investigations with the characteristic fluid mechanical phenomena of boundary layer separation and reattachment addressed for example in [18]. To suppress the pressure-induced separation bubble present at specific diffuser angles, ASC by means of steady or unsteady jets can be applied, where generally three operating parameters need to be chosen:

- the ratio of jet and free stream velocity $r = u_{\text{jet}}/U_{\infty}$ corresponding to the momentum input,
- the jet emission angle φ , enclosed by the direction of the jet and the wall and
- the reduced forcing frequency $F^+ = (fL)/U_{\infty}$ associated with the frequency of the unsteady jet f (if applicable) and the control length L .

✉ B. Steinfurth
ben.steinfurth@tu-berlin.de
F. Haucke
frank.haucke.1@tu-berlin.de
J. Weiss
julien.weiss@tu-berlin.de

¹ Technische Universität Berlin, Berlin, Germany

While steady blowing is successfully applied to control the flow along a backward facing ramp in [1, 11] (amongst others), pulsed blowing is deemed to be both more effective and more efficient [4].

Out of the stated operating parameters that need to be chosen for separation control experiments, the forcing frequency characterizing the periodic process, appears to be the least sensitive for relatively small actuation intensities applied on a diffuser flow, as its variation may only yield slight deviations of the actuation effectivity [10]. Furthermore, often times, there is no rigorous verification as to whether an improved performance is down to flow receptivity or actuator characteristics when the frequency is varied.

Setting the velocity ratio, on the other hand, can be more challenging as a sufficient momentum input needs to be ensured while an excessive energy consumption has to be avoided [10]. A cylindrical model exhibiting an axisymmetric afterbody with a backward facing ramp, is investigated in [19]. It is shown that the emission of compressed air through slots located slightly downstream of the separation point yields a complete suppression of the recirculation bubble at a velocity ratio of $r = 1.55$ for the studied scenario. This is attributed to an effective manipulation of the shear layer.

Besides the velocity ratio, the jet introduction angle is crucial in terms of effective ASC. Generally, a steep jet emission may be employed to generate large-scale vortex structures due to an interaction with the crossflow, shifting high-momentum fluid toward the wall. In comparison, a small emission angle aims at a direct energization of the boundary layer. Thus, the aerodynamic performance can be improved utilizing various ASC devices [12]. Representing a preliminary study of the present article, an experimental investigation of pulsed jets emitted through slots is documented for different emission angles in [7]. It is shown that for emission angles of $\varphi = [30^\circ, 60^\circ]$, the jet is immediately attached to the wall, not producing as large vortex structures as for $\varphi = 90^\circ$. An experimental parametric study regarding ASC on a one-sided diffuser via active vortex generators is presented in [3]. It is found that a jet introduction against the free stream direction becomes ever more efficient with increasing velocity ratios while blowing downstream is optimal for velocity ratios of $1.5 \leq r \leq 2.5$.

Evidently, ASC regarding the flow along a one-sided diffuser is generally feasible. However, no clear strategy is presented when the actuation parameters are concerned. This is ascribed to an incomplete knowledge of physical events caused by varying operating conditions of the deployed devices. This article contributes to improve the understanding of flows manipulated by fluidic actuators. The objective is the assessment of mechanisms associated with fluidic oscillators (FOs) and fluidic diverters (FDs), employed with equal actuation intensities and jet emission angles. For this purpose, the three-component velocity field

in multiple cross-sections as well as the wall pressure distributions induced by the investigated fluidic actuators are studied. Furthermore, proper orthogonal decomposition (POD) is deployed to reveal dominant flow structures that enable conclusions regarding the flow control authority of the fluidic devices.

2 Methods

In this chapter, the experimental setup and procedure are introduced. Then, basic background knowledge regarding the method of POD is imparted.

2.1 Experimental setup

The experiments were conducted in a subsonic closed-loop wind tunnel with a maximum turbulence intensity of $Tu \approx 0.8\%$ inside the cross-section at the diffuser opening. To establish a turbulent boundary layer on the test section floor, roughness elements were placed at the entrance of the test section and the free stream Reynolds number was set to $Re_\infty = 550,000$ based on the ramp control length $L \approx 0.35$ m. The boundary layer shape factor was of the order of $H = 1.36$, which indicates a turbulent state. The adjustable diffuser opening angle was set to $\alpha = 21^\circ$, ensuring pressure-induced flow separation at $x/L \approx 0.2$ with the actuator outlet located slightly upstream at $x/L \approx 0.12$. The test section is depicted schematically in Fig. 1.

The internal geometries of the fluidic actuators that were investigated independently, are shown in Fig. 2.

In the case of the FD, two alternately pulsed jets were emitted through slots with an aspect ratio of $d/b = 31.5$, where d is the length and b the width of the slots. This was achieved by periodically deflecting compressed air coming

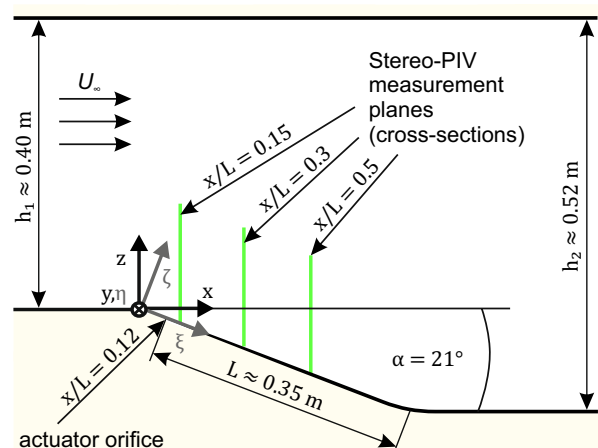


Fig. 1 Experimental setup inside test section

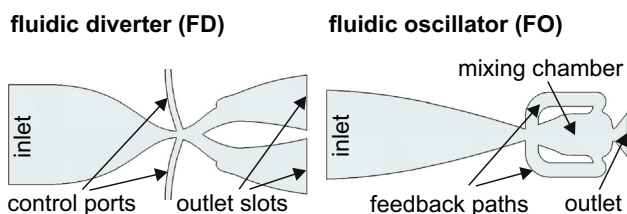


Fig. 2 Internal geometries of fluidic actuators studied

from the plenum with the help of significantly smaller control mass flows. While self-oscillating FDs have been successfully applied in the field of ASC [2], a solenoid valve controlled by a signal generator was utilized to feed the control ports alternately with a constant actuation frequency within the frame of the present study.

On the contrary, the FO generated a spatially oscillating jet emitted from an orifice with a much smaller aspect ratio of $d/b \approx 0.6$ and a sweeping angle of $\vartheta \approx 85^\circ$ that is spanned by the end positions of the oscillation motion.

The function principle of the device is based on the jet introduced into the internal mixing chamber attaching on one side due to the Coanda effect. A portion of the fluid then is redirected through the respective feedback path and interacts with the air at the inlet of the mixing chamber, deflecting it toward the other side before the cycle repeats. For extensive reviews of FO design and application, the reader is referred to [5, 16].

Exemplary time signals of the normalized total pressure $p_t/p_{amb}(t)$ at the center of both actuator outlets are shown in Fig. 3. Note that the studied FO device generates a naturally oscillating jet with an inconstant amplitude, although at a frequency much greater than achieved by the investigated FD.

The unequal frequencies investigated for the two devices in this study reflect typical ASC applications where sweeping frequencies for FOs are usually greater than pulse frequencies for pulsed-jet actuators of a similar size. Also, it

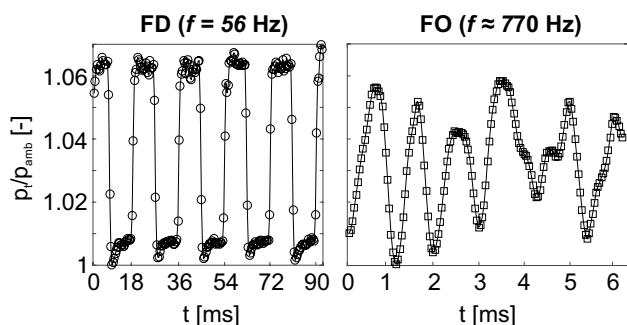


Fig. 3 Normalized total pressure (time signal) at respective center of actuator outlets, devices supplied with same mass flow rate; left: FD, right: FO

should be noted that the frequency is associated with different vortex formations mechanisms for both actuators. Therefore, keeping this specific parameter constant would not necessarily result in equal excitation conditions. The reduced frequency associated with the pulsed jets emitted by the studied FD device is of the order of $F^+ = 0.8$, which lies within the range of effective forcing frequencies stated in [4]. The sweeping frequency of the FO yields reduced frequencies of $F^+ \approx [5.4, 10.9]$, which correspond to the studied velocity ratios.

The remaining parameter space is spanned by three jet introduction angles relative to the ramp surface downstream of the outlet ($\varphi = [30^\circ, 60^\circ, 111^\circ]$) and two different velocity ratios ($r = [1.6, 3.3]$). The jet velocities both for the FD and for the FO device were estimated based on the mean mass flow rate assuming incompressibility. Since the outlet areas of the two actuator devices were of the same size, equal velocity ratios were associated by equal actuation intensities, i.e., momentum coefficients.

Information regarding the velocity fields was gathered in cross-sections located at $x/L = [0.15, 0.3, 0.5]$. A dual pulsed laser with an energy set to $E \approx 75$ mJ per pulse was employed to illuminate DEHS particles of $d = 1 \dots 3$ μm diameter. The pulse delay of the order of $\Delta t_{pd} = 8 \dots 10$ μs was set to ensure distinct correlation peaks while avoiding out-of-plane motion of seeding particles. Two *pco.edge* CMOS cameras boasting a resolution of $[2560 \times 2160]$ px², were arranged in stereoscopic configuration (2D-3C). The spatial resolution of the measured velocity data is stated in Table 1. To tackle the effect of laser light reflection off the diffuser surface and obtain velocity data close to the wall, a foil was applied to the surface, emitting light of a wavelength that could be filtered. Thus, the influence of reflections was minimized and successful image correlation performed up to the wall distance noted in Table 1.

For each configuration, 2000 double images were recorded per camera with a constant frequency of $f = 5$ Hz. Multiple FFT correlation as well as interrogation grid refinement were employed to evaluate the raw data before applying sophisticated outlier detection schemes. The proportion of valid data was consistently above 94 % with implausible data replaced by lower order peaks and interpolated vectors respectively.

Table 1 Properties of acquired velocity data fields at different stream-wise positions

Position $x/L [-]$	Spatial resolution $\Delta y = \Delta z$ [mm]	Wall distance h_z [mm]
0.15	0.56	0.84
0.3	0.75	1.38
0.5	0.94	3.20

The wall pressure distribution on a section of the one-sided diffuser was obtained through 24 pressure taps displayed in Fig. 4. Differential pressure sensors with a maximum error of $|\text{err}_p| = 3.75 \text{ Pa}$ were utilized and sampled with a rate of $f = 250 \text{ Hz}$ during the respective PIV measurement interval $\Delta t = 400 \text{ s}$.

Note that only time-averaged pressure distributions are discussed as no spectral analysis is conducted in this study. With regards to pressure distributions, symmetry was assumed so that pressure coefficients

$$c_p(\xi, \eta) = \frac{p_{\text{stat}}(\xi, \eta) - p_\infty}{q_\infty} \quad (1)$$

are mirrored around the symmetry plane ($\eta/L = 0$). The symmetrical generation of the actuator jets was validated in a preliminary study.

2.2 Background on proper orthogonal decomposition

When investigating turbulent flows, one is generally confronted with a superposition of multiple dynamical events. The method of POD, as introduced in [13, 17], provides a tool for decomposing flow configurations into energetically dominant spatial and temporal features. This is achieved by determining an optimal base to represent a given data set based on the L_2 norm. In the present scenario, snapshot POD was employed on the basis of velocity fields at different time instances, which were decomposed into a mean and a fluctuating component

$$U(\mathbf{x}, t) = \bar{\mathbf{u}}(\mathbf{x}) + \mathbf{u}'(\mathbf{x}, t). \quad (2)$$

The fluctuating part was approximated by the sum of products of spatial modes Φ_i and related temporal mode coefficients a_i :

$$\mathbf{u}'(\mathbf{x}, t) = \sum_{i=1}^N \Phi_i(\mathbf{x}) a_i(t) + \mathbf{u}'_{\text{res}}(\mathbf{x}, t) \quad (3)$$

with N snapshots provided by PIV measurements. To find these spatial modes and mode coefficients subject to a minimized residual $\mathbf{u}'_{\text{res}}(\mathbf{x}, t)$, the symmetric, positive semi-definite correlation matrix was computed using the L_2 inner product:

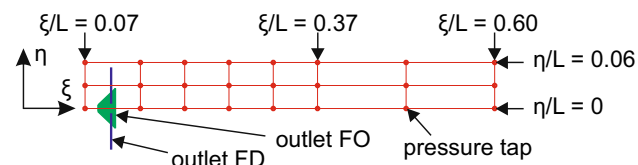


Fig. 4 Actuator outlets and grid of pressure taps; for orientation of ξ, η, ζ coordinate system, refer to Fig. 1

$$\mathbf{R}_{ij} = \frac{1}{N} \langle \mathbf{u}'(\mathbf{x}, t_i), \mathbf{u}'(\mathbf{x}, t_j) \rangle. \quad (4)$$

Then, the mode coefficients a_i as well as the eigenvalues λ_i were found by solving the eigenvalue problem

$$\mathbf{R} \mathbf{a}_i = \lambda_i \mathbf{a}_i. \quad (5)$$

The real, non-negative eigenvalues, representing twice the amount of turbulent kinetic energy contained in each mode, were sorted by magnitude and the spatial modes then obtained by projecting the snapshots onto the mode coefficients, i. e., the eigenvectors:

$$\Phi_i(\mathbf{x}) = \frac{1}{N \lambda_i} \mathbf{a}_i(t_j) \mathbf{u}'(\mathbf{x}, t_j). \quad (6)$$

By construction, these modes are orthonormal and based on the amount of energy contained.

3 Results and discussion

The following section presents the main results of the conducted investigations. While doing so, the time-averaged velocity fields and wall pressure distributions induced by the fluidic devices are touched upon. Subsequently, the computed spatial POD modes are discussed and the influence of a velocity ratio variation is evaluated. Finally, the dynamical behavior of the manipulated flow fields is reconstructed by means of the obtained temporal POD coefficients, allowing for a brief analysis of the development of induced vortex structures.

3.1 Time-averaged velocity fields

In the following section, the manipulated velocity distribution inside the mentioned transverse measurement planes is assessed. Focusing on results for varied actuator emission angles at a velocity ratio of $r = 3.3$. Note that the outlined flow phenomena are similarly present at lower velocity ratios, albeit to a lesser extent.

The uncontrolled base flow inside the three cross-sections is depicted in Fig. 5. A shear layer homogenous in y -direction can be identified at $x/L = 0.15$. Further downstream at $x/L = 0.3$ and $x/L = 0.5$, a slight asymmetry develops with the time-averaged separation bubble visible at $y/L < 0$ inside the central transverse plane. In preliminary investigations, the mean separation point was determined to be located at $x/L \approx 0.2$.

The influence of two alternately pulsed jets emitted by the FD device is depicted in Fig. 6. It can be noted that the velocity deficit is generally reduced through actuation. This is especially true for emission angles $\varphi = [30^\circ, 60^\circ]$, where a distinct downwash is induced at $x/L = 0.15$. On the contrary,

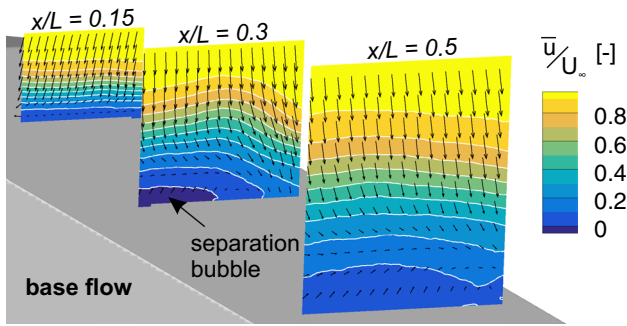


Fig. 5 Distribution of normalized velocity inside transverse measurement planes for base flow scenario

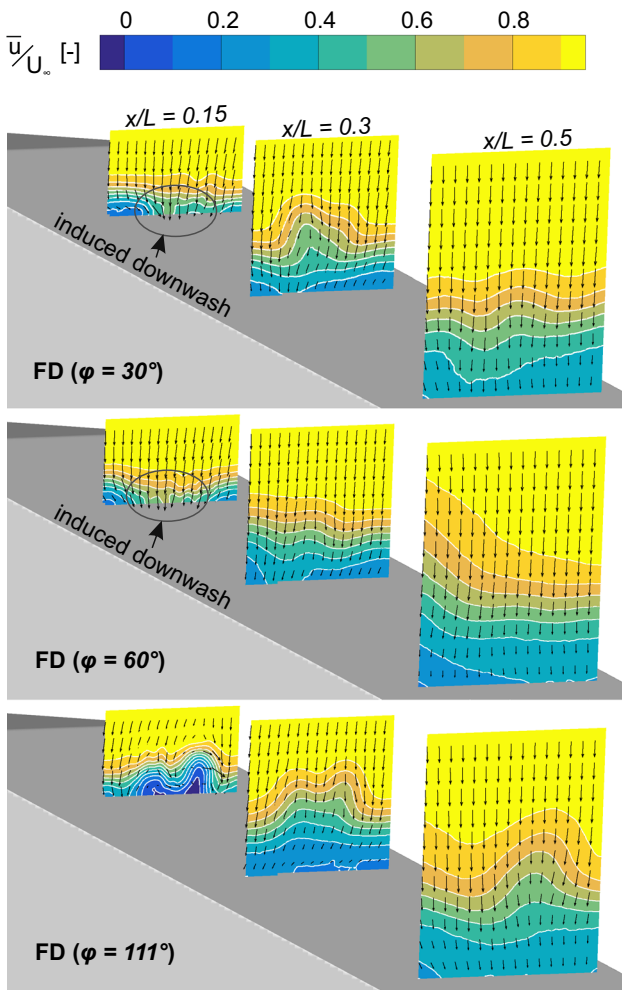


Fig. 6 Influence of varied emission angle of FD on normalized time-averaged streamwise velocity component (contour) and transverse components (vectors) in three cross-sections at velocity ratio $r = 3.3$

the steeper jet introduction yields two distinct wakes, exhibiting streamwise vortices and recirculation. This behavior is attributed to the direction of momentum input, which is locally against the flow direction, damming the oncoming

fluid and generating a wake flow similar to solid bodies. The ensuing velocity deficit is still present further downstream, although damped due to viscosity.

Figure 7 illustrates the effect of a sweeping jet generated by the studied FO on the one-sided diffuser flow. Similar to the investigated FD, the velocity magnitude is increased in the case of all emission angles. There is no recirculation area found in any of the evaluated cross-sections. Likewise, the actuation at jet introduction angles of $\varphi = [30^\circ, 60^\circ]$, representing a momentum increase through direct injection, yields significant velocity gains in the center of the measurement planes at $x/L = 0.15$. However, as opposed to the downwash seen in Fig. 6 for the FD at $\varphi = 60^\circ$, an outward rotating vortex pair is found for the FO, producing a slight deficit in \bar{u}/U_∞ further downstream. Actuation with the steepest emission angle $\varphi = 111^\circ$ produces a similar counter-rotating vortex pair but a distinct velocity deficit is found already at $x/L = 0.15$. The general effect leading to the wake flow character is the same as for the FD outlined

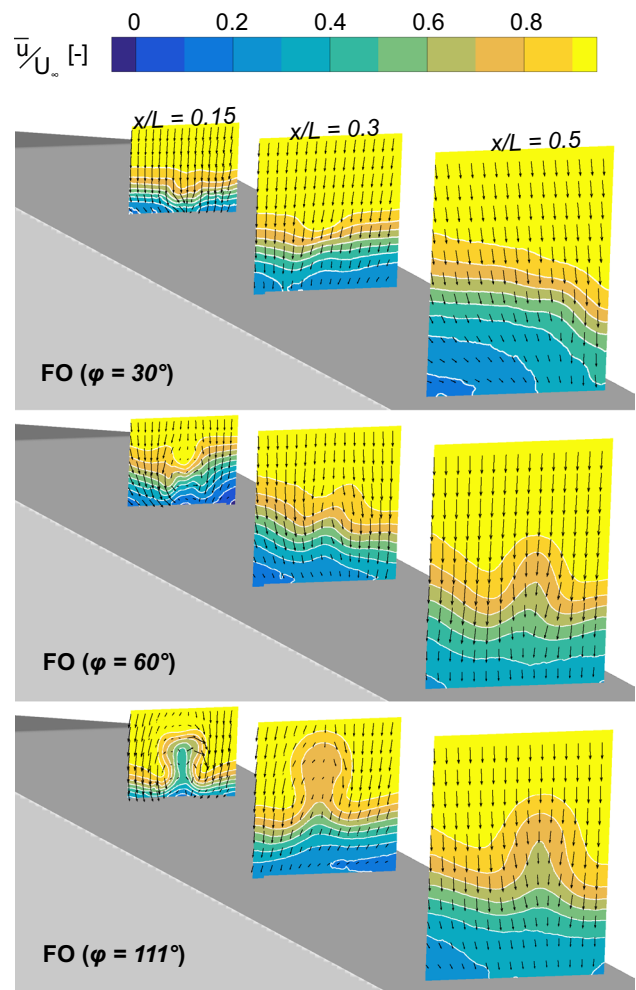


Fig. 7 The same as Fig. 6 but related to actuation with FO device

above. However, a steeper jet trajectory can be noted, which is ascribed to the greater outlet width of the FO, and thus delayed dissipation of the sweeping jet. Furthermore, no recirculation is found at $x/L = 0.15$.

3.2 Time-averaged wall pressure distribution

In this section, the ensuing wall pressure distributions, corresponding to the velocity fields discussed above, are presented.

Figure 8 shows the distribution associated to the base flow. The positions furthest upstream exhibit pressure coefficients of $c_p < 0$, which can be attributed to a flow deflection and acceleration at the diffuser opening. Further downstream, the pressure coefficient increases slightly. However, a large coherent region of constant pressure is present, spanning from $\xi/L \approx 0.16$ to $\xi/L \approx 0.54$. This represents a strong indicator of flow separation and partly corresponds with the results related to the conducted velocity measurements, see Fig. 5.

The wall pressure distribution subject to actuation by an FD device at the studied jet emission angles and a constant velocity ratio of $r = 3.3$ is shown in Fig. 9. Generally, there is a similar pressure recovery noticeable in all cases as coefficients of $c_p > 0$ are achieved already at $\xi/L < 0.4$. Furthermore, there are regions of significant pressure deficit close to the actuator outlets visible. These areas are especially pronounced in the case of $\varphi = 111^\circ$, where an assumed damping of crossflow fluid and bending of pathlines results in a significantly reduced static pressure.

The corresponding wall pressure distributions induced by actuation through an FO are shown in Fig. 10. While the effect of emission at an angle of $\varphi = 30^\circ$ is marginal, the other cases yield greater wall pressure at $\xi/L > 0.5$, although at the cost of reduced pressure coefficients further upstream. Compared to the wall pressure distribution produced by the FD, the pressure increase downstream is countered by the fact that the pressure deficit close to the actuator is significantly smaller.

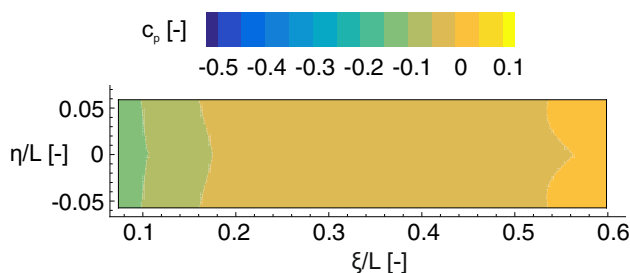


Fig. 8 Distribution of pressure coefficient associated to base flow (no actuation applied) measured with 8×3 grid of pressure taps

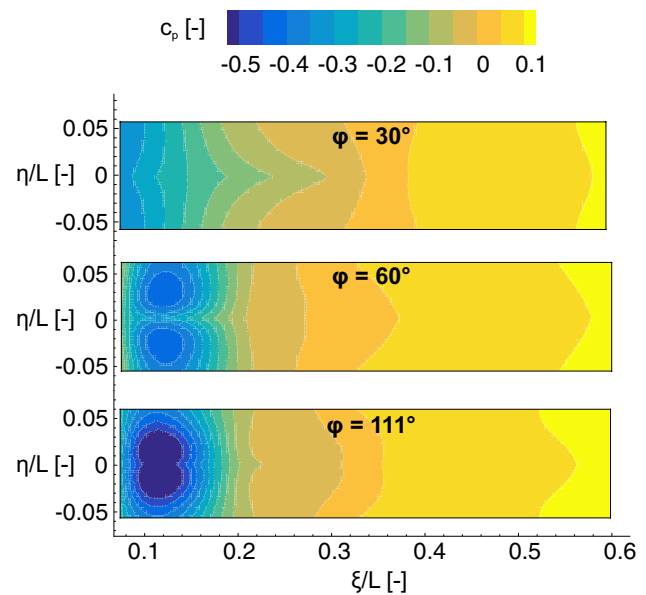


Fig. 9 Wall pressure distribution induced by pulsed jets generated by an FD at different emission angles and constant velocity ratio $r = 3.3$ measured with 8×3 grid of pressure taps

3.3 Spatial POD modes

The spatial POD modes associated with the streamwise velocity component are presented in the following. In the course of discussing the results, the modal properties present at the lower momentum input ($r = 1.6$) are compared with the behavior related to the greater velocity ratio $r = 3.3$.

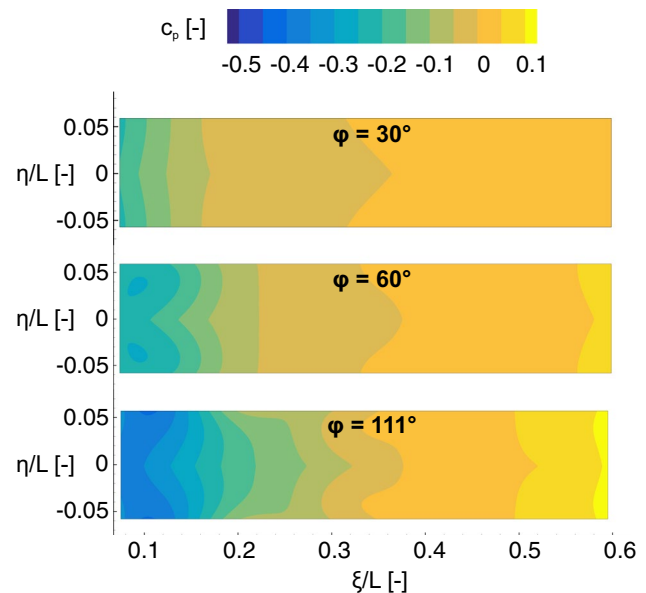


Fig. 10 The same as Fig. 9 but related to actuation with FO device

Thus, flow structures produced by different velocity ratios are unveiled.

With the exception of the base flow scenario, the focus is laid upon the measurement plane at $x/L = 0.3$.

Note that the turbulent kinetic energy contained in each mode is stated as a fraction of the total fluctuating energy

$$TKE = \sum_{i=1}^N TKE_i = \frac{1}{2} \sum_{i=1}^N \lambda_i. \tag{7}$$

3.3.1 Base flow

The uncontrolled flow is represented by a first spatial mode describing the shear layer enclosed by the free stream and low-energy flow in closer wall proximity (Fig. 11). This mode contains consistently at least 30 % of the total turbulent kinetic energy across all three measurement planes and is supplemented by a higher harmonic in the second mode, boasting about one fourth of the turbulent kinetic energy related to the first mode.

3.3.2 Fluidic diverter

Actuation by means of an FD at a jet introduction angle of $\varphi = 30^\circ$ and the smallest studied velocity ratio yields a first mode similar to the first base flow mode, although the border between free stream and the region of velocity deficit is displaced toward the wall (Fig. 12). The greater actuation intensity produces a pair of modes which are similar in structure but contain significantly differing amounts of fluctuating energy. A structure corresponding to the base flow is not present, however, which can be attributed to the more pronounced flow alteration at $r = 3.3$.

The most dominant spatial POD modes subject to ASC with an FD at an emission angle of $\varphi = 60^\circ$ are depicted in Fig. 13. The flow configuration at the smaller velocity ratio again is dominated by a spatial mode similar to the one describing the base flow case. The other modes represent the dynamical process of the two alternately pulsed jets but are

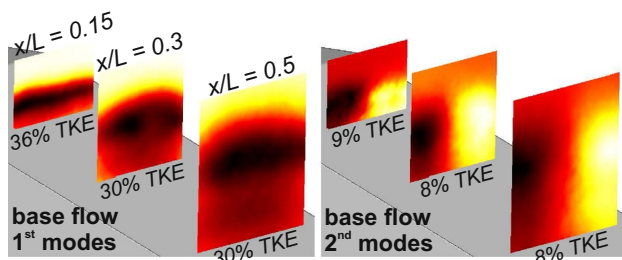


Fig. 11 First and second spatial modes representing the streamwise velocity component of the one-sided diffuser base flow

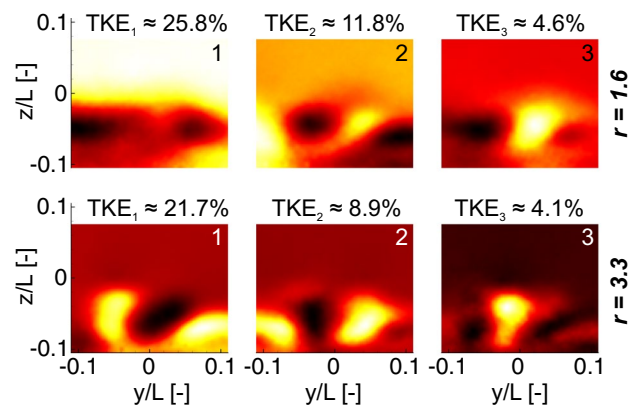


Fig. 12 Three most dominant spatial modes induced by FD at $\varphi = 30^\circ$ and $x/L = 0.3$; top row: velocity ratio $r = 1.6$, bottom row: $r = 3.3$; colormap within the range of $u/\max(u) = [-0.1, 0.1]$

associated with significantly less turbulent kinetic energy. Increasing the momentum input produces a displacement of observable structures toward the diffuser wall. Additionally, the base flow mode is diminished as was the case at an emission angle of $\varphi = 30^\circ$ discussed above.

The same is applicable to the configuration exhibiting the steepest emission angle $\varphi = 111^\circ$, which is displayed in Fig. 14. The two most dominant modes corresponding to an increased velocity ratio represent a smaller fraction of the total kinetic energy (Fig. 15), which may be ascribed to a suppression of the base flow mode.

3.3.3 Fluidic oscillator

The spatial POD modes generated by actuation through an FO device at an emission angle of $\varphi = 30^\circ$ are depicted in Fig. 16. The spatial modes describe the dynamical process defined by the generated sweeping jet. It can be noted that the effect of the varied velocity ratio is marginal with

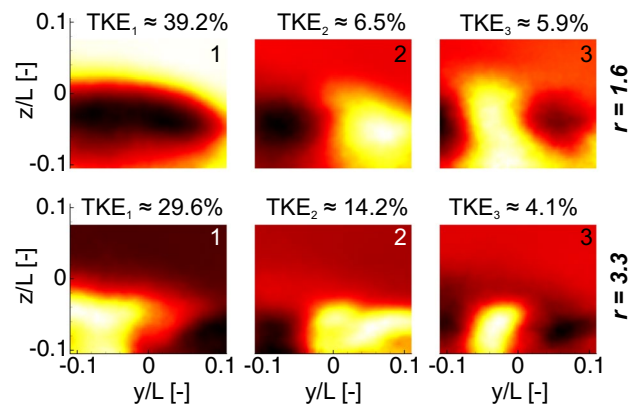


Fig. 13 The same as Fig. 12 but emission angle set to $\varphi = 60^\circ$

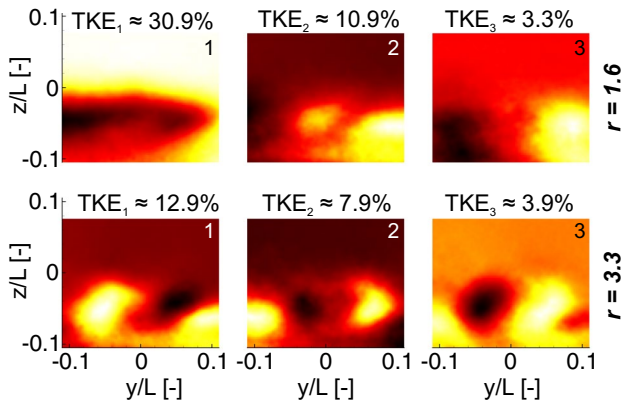


Fig. 14 The same as Fig. 12 but emission angle set to $\varphi = 111^\circ$

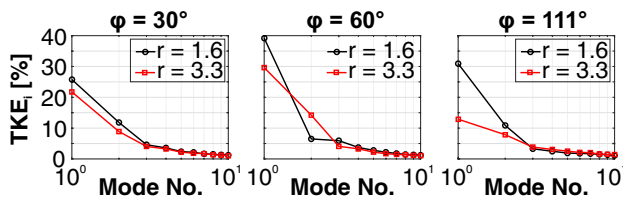


Fig. 15 Mode spectra of one-sided diffuser flow manipulated by FD at $x/L = 0.3$ subject to varied emission angle and velocity ratio; first 10 modes shown (logarithmic scale)

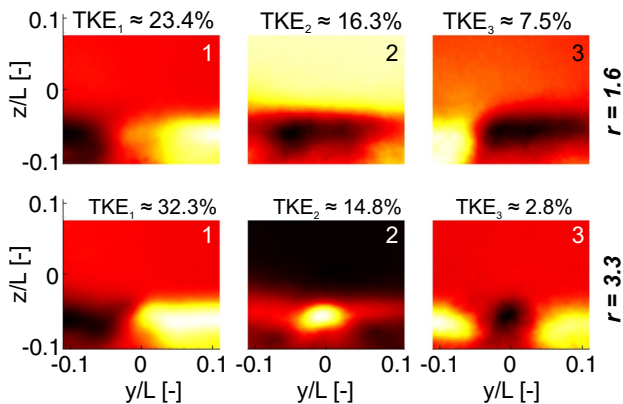


Fig. 16 Three most dominant spatial modes induced by FO at $\varphi = 30^\circ$ and $x/L = 0.3$; top row: velocity ratio $r = 1.6$, bottom row: $r = 3.3$

the most dominant mode remaining generally unchanged. When compared to the base flow case, the flow structures are located in closer proximity to the wall. This underlines the positive effect of the applied actuation with regards to flow separation and agrees well with the velocity field shown in Fig. 7.

Jet introduction at an angle of $\varphi = 60^\circ$ yields a dominant mode that is comparable to the base flow, containing

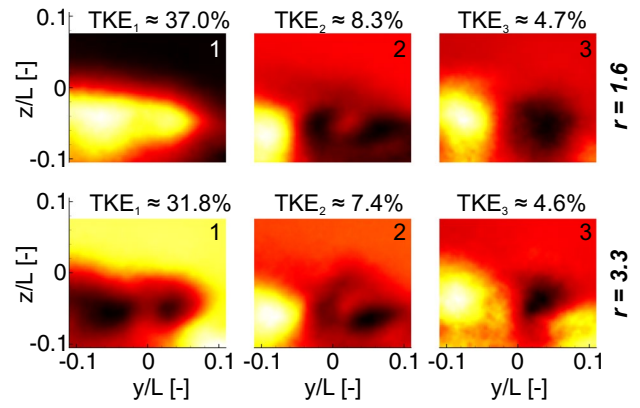


Fig. 17 The same as Fig. 16 but emission angle set to $\varphi = 60^\circ$

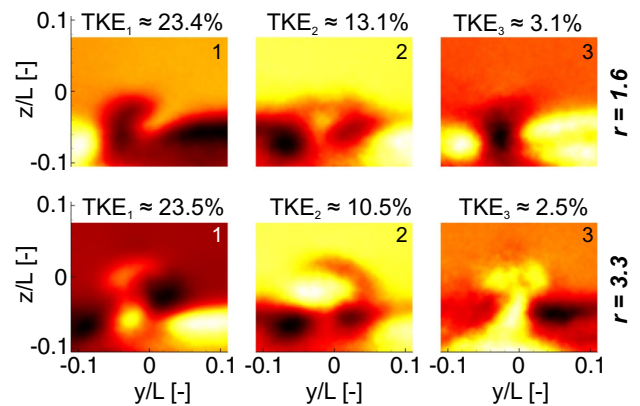


Fig. 18 The same as Fig. 16 but emission angle set to $\varphi = 111^\circ$

about one third of the total fluctuating energy at both assessed velocity ratios (Fig. 17). The second and third spatial modes are structurally unaltered as well and represent a similar fraction of turbulent kinetic energy across different velocity ratios. Generally, the effect of velocity variation appears to be the least significant in the case of FO application at $\varphi = 60^\circ$ when the spatial POD modes are concerned.

The steepest emission angle $\varphi = 111^\circ$ produces spatial modes, which reflect the slightly asymmetrical penetration of the sweeping jet into the diffuser flow, see Fig. 18. While the displayed structures again are generally similar and contain a comparable amount of fluctuating energy, there are coherent regions in the center of the cross-section observable at $r = 3.3$ that are not present at the lower momentum input. This finding can be explained by the steeper trajectory corresponding to the greater velocity ratio.

Similar to the one-sided diffuser flow manipulated by an FD device, the modal behavior induced by the FO is mainly defined by two dominant spatial modes. However, an increase of the velocity ratio does not yield flattened mode

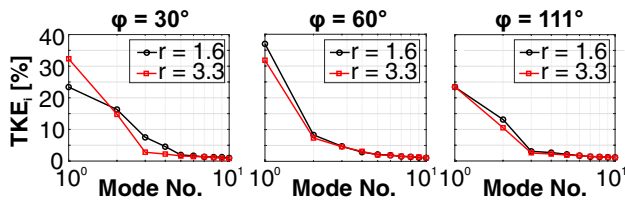


Fig. 19 Mode spectra of one-sided diffuser flow manipulated by FO at $x/L = 0.3$ subject to varied emission angle and velocity ratio; first 10 modes shown (logarithmic scale)

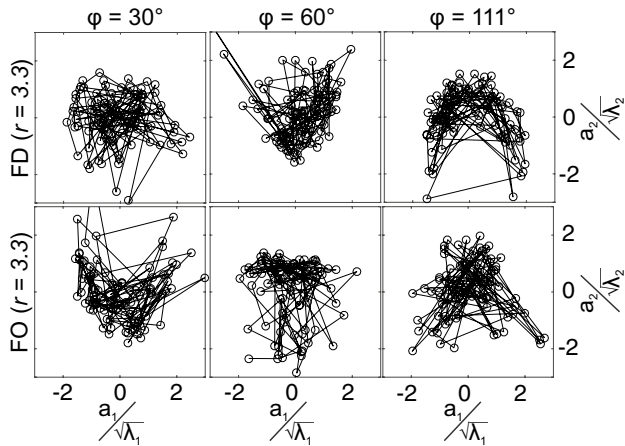


Fig. 20 Phase portraits stemming from the first 150 temporal coefficients corresponding to first two modes at different emission angles, $x/L = 0.15$, $r = 3.3$; top row: induced by FD, bottom row: induced by FO

spectra. In fact, the influence of a varied actuation intensity is rather marginal as shown in Fig. 19.

3.4 Reduced order model of dynamical behavior

The scaling of spatial modes discussed above is carried out by means of temporal coefficients a defined as eigenvectors solving the eigenvalue problem stated in equation (4). Note that each mode coefficient is related to a spatial mode and to a specific snapshot, i. e., an instance in time.

Assuming that the flow fields manipulated both by the FD and the FO, exhibit $T = 2\pi$ periodic limit cycle behavior and are defined by two dominant modes oscillating with a phase shift of π , the phase portraits of these modes, depicted in Fig. 20, are expected to yield circular point clouds.

Since all measurement cases are rather heavily subsampled, the connecting lines of neighboring coefficient pairs do not describe a curve. However, this does not prevent a recovery of phase information, which is performed by computing the phase angle Ψ of each mode coefficient tuple regarding a circle with a center at $(a_1, a_2) = (0, 0)$, as carried out in, for example, [14]. By superposing the two most dominant modes for

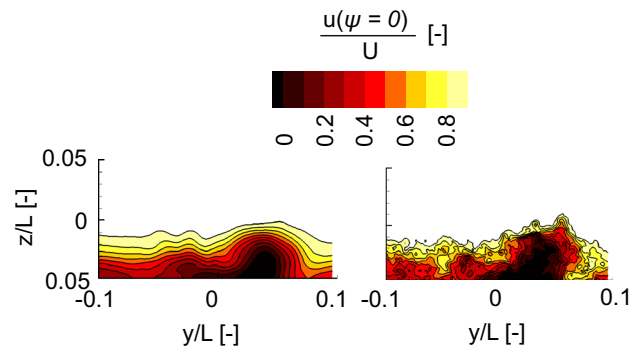


Fig. 21 Streamwise velocity field at phase angle $\Psi = 0$ subject to actuation by means of FD device at $x/L = 0.15$, $\varphi = 111^\circ$, $r = 3.3$, left: phase-averaged and superposition of first two modes, right: snapshot related to the same phase angle

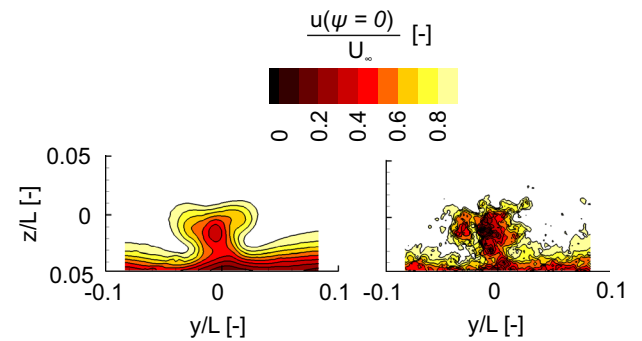


Fig. 22 The same as Fig. 21 but actuation by means of FO device

the investigated flow fields according to equation (2), reduced order models were deduced with most of the incoherent noise being eliminated. This was further enhanced by phase averaging within appropriate phase angle windows of the order of $\Delta\Psi = \pi/12$.

The benefit of the obtained reduced order models is illustrated by Figs. 21 and 22, where the mean streamwise velocity component obtained from superposing the first two modes is compared to an exemplary snapshot related to the same phase angle. On the basis of visual inspection, it can be noted that the phase information is reproduced precisely while incoherent noise is reduced.

Further results of the obtained reduced order models are presented exemplarily in the following, focusing on the dynamical behavior of vortex structures inside the cross-section at $x/L = 0.15$ induced by the greatest momentum input at $r = 3.3$ and an emission angle of $\varphi = 111^\circ$.

As a means of vortex identification, the Q-criterion introduced in [9], is applied where the streamwise component for each spatial point is given by

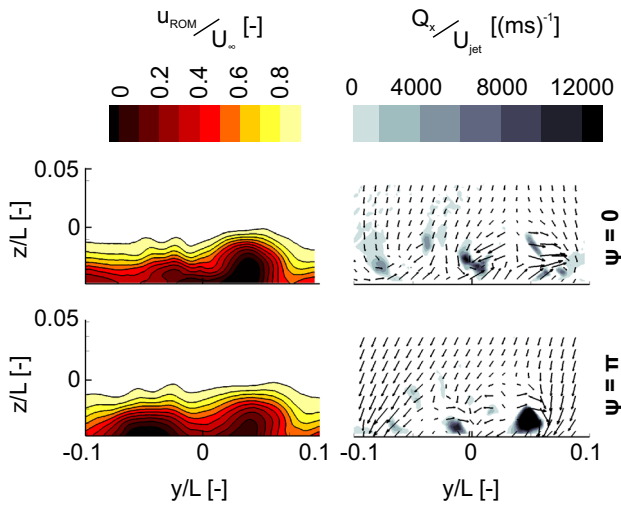


Fig. 23 Flow structures induced by FD device at $x/L = 0.15$, $\varphi = 111^\circ$, $r = 3.3$ during two phases $\Psi = 0$ (top row) and $\Psi = \pi$ (bottom row); left column: normalized streamwise velocity, right column: normalized Q-criterion indicator

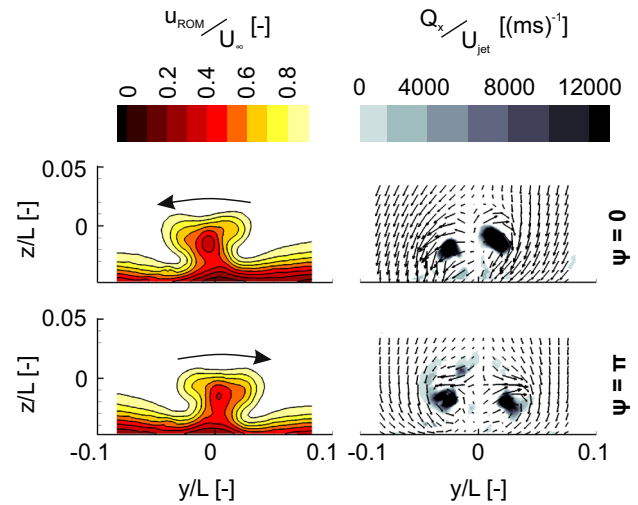


Fig. 24 The same as Fig. 23 but due to actuation by means of FO device

$$Q_x = -\frac{1}{2} \left[\left(\frac{\partial v}{\partial y} \right)^2 + \left(\frac{\partial w}{\partial z} \right)^2 \right] + \frac{\partial v}{\partial y} \frac{\partial w}{\partial z} - \frac{\partial v}{\partial z} \frac{\partial w}{\partial y}. \quad (8)$$

Positive values of Q_x represent areas where the vorticity magnitude is greater than the shear strain rate so that coherent regions with this property represent vortices. These flow structures, as generated by the studied FD, are shown in Fig. 23. The observed vortex structures are located at the edges of the actuator slot. As can be assumed from the velocity distribution, the momentum input through the two slots differs with the orifice at $y/L > 0$ producing more significant vortices. While they are shown to oscillate with respect to the phase angle, the velocity deficit associated to the emitted jet at $y/L > 0$ is still present during the emission phase of the other actuator slot $\Psi = \pi$. The vortex structures indicated by the Q-criterion are even more distinct then.

Longitudinal vortices generated by the FO operated at an emission angle of $\varphi = 111^\circ$ are displayed in Fig. 24. It can be noted that the sweeping character of the jet is reproduced by scaling the first two modes with the related POD coefficients. The induced velocity deficit is deflected to opposite sides during the shown phase angles. Compared to the actuation by means of the FD, the generated vortex structures are more distinct and further detached from the wall. Both findings can be attributed to the greater jet diameter in the case of the FO, enabling greater penetration depth at an equal momentum input.

4 Conclusions

The present article documents a modal analysis of experimentally obtained data regarding ASC experiments on a one-sided diffuser. Two fluidic actuators were investigated and flow fields subject to emitted jets of different characteristics were compared. It was found that at a low velocity ratio of $r = 1.6$, two alternately pulsed jets (FD) yield a dominant spatial mode that resembles the uncontrolled flow. However, this feature was suppressed at a greater velocity ratio $r = 3.3$ and replaced by structures that describe the jet pulsation. As for the studied FO device, the effect of a varied momentum input on the spatial modes was found to be marginal.

Apart from a steeper jet trajectory, actuation at greater emission angles also produced more distinct vortex structures due to a more pronounced interaction with the cross-flow for both devices. This resulted in a momentum shift toward the diffuser wall. However, steeper jet introduction also lead to significant damming of fluid, generating regions of velocity deficit inside the jet wakes.

In regard to the technical application of fluidic devices, more distinct longitudinal vortex structures were found for the FO at the same momentum input. Furthermore, an elimination of the base flow mode observed in the case of the FD, suggests that a threshold in actuation intensity needs to be surpassed to ensure sufficient control authority. The choice of emission angle has to factor in the short-term loss in the form of a velocity deficit but ultimately greater wall pressure present at steep emission angles against a continuous increase of pressure in the case of flatter emission angles.

References

1. Ball, W.H.: Tests of wall blowing concepts for diffuser boundary layer control. In: 20th Joint Propulsion Conference (1984)
2. Bauer, M., Lohse, J., Haucke, F., Nitsche, W.: High-lift performance investigation of a two-element configuration with a two-stage actuator system. *AIAA J.* **52**(6) (2014)
3. Cuvier, C., Braud, C., Foucaut, J.M., Stanislas, M.: Flow control over a ramp using active vortex generators. In: 7th International Symposium on Turbulence and Shear Flow Phenomena (2011)
4. Greenblatt, D., Wygnanski, I.J.: The control of flow separation by periodic excitation. *AIAA J.* **36**, 487–545 (2000)
5. Gregory, J.W., Tomac, M.N.: A review of fluidic oscillator development and application for flow control. In: 43rd Fluid Dynamics Conference, AIAA (2013)
6. Guyot, D., Bobusch, B., Paschereit, C.O., Raghu, S.: Active combustion control using a fluidic oscillator for asymmetric fuel flow modulation. In: Proceedings of the 44th AIAA/ASME/SAE/ASEE Joint Propulsion Conference & Exhibit (2008)
7. Hecklau, M., Salazar, D.P., Nitsche, W.: Influence of the actuator jet angle on the reattachment process with pulsed excitation. Notes on Numerical Fluid Mechanics and Multidisciplinary Design, vol 121 (2010)
8. Hossain, M.A., Prenter, R., Lundgreen, R.K., Ameri, A., Gregory, J.W., Bons, J.P.: Experimental investigation of sweeping jet film cooling. In: Proceedings of ASME Turbo Expo 2017, Turbomachinery Technical Conference and Exposition (2017)
9. Hunt, J.C.R., Wray, A.A., Moin, P.: Eddies, stream, and convergence zones in turbulent flows. In: Center for Turbulence Research Report CTR-S88 (1988)
10. Joseph, P., Bortolus, D., Grasso, F.: Flow control on a 3D backward facing ramp by pulsed jets. *C. R. Mecanique* **342**(6-7) (2014)
11. Kumar, V., Alvi, F.S.: Use of high-speed microjets for active separation control in diffusers. *AIAA J.* **44**(2) (2006)
12. Lenkins, L., Gorton, S.A., Anders, S.: Flow control device evaluation for an internal flow with an adverse pressure gradient. In: 40th AIAA Aerosp. Sci. Meet. Exhibit (2002)
13. Lumley, J.L.: *Stochastic Tools in Turbulence*. Academic, New York (1970)
14. Perrin, R., Braza, M., Cid, E., Cazin, S., Barthet, A., Sevrain, A., Mockett, C., Thiele, F.: Phase averaged turbulence properties in the near wake of a circular cylinder at high Reynolds number using POD. In: 13th Int Symp on Applications of Laser Techniques to Fluid Mechanics (2006)
15. Phillips, E., Wozidlo, R., Wygnanski, I.: Separation control on a dynamic trailing-edge flap. In: AIAA 5th Flow Control Conference (2010)
16. Raghu, S.: Fluidic oscillators for flow control. *Exp. Fluids* **54**(2) (2013)
17. Sirovich, L.: Turbulence and the dynamics of coherent structures. Part I: Coherent structures. *Quart. Appl. Math.* **45**(3) (1987)
18. Song, S., DeGraaff, D.B., Eaton, J.K.: Experimental study of a separating, reattaching, and redeveloping flow over a smoothly contoured ramp. *J. Heat Fluid Fl.* **21**(5) (2000)
19. Viswanath, P.R., Ramesh, G., Madhavan, K.T.: Separation control by tangential blowing inside the bubble. *Exp. Fluids* **29**(1) (2000)